

Artificial Intelligence Resolves Kinetic Pathways of Magnesium Binding to RNA

Jan Neumann and Nadine Schwierz*



Cite This: *J. Chem. Theory Comput.* 2022, 18, 1202–1212



Read Online

ACCESS |



Metrics & More

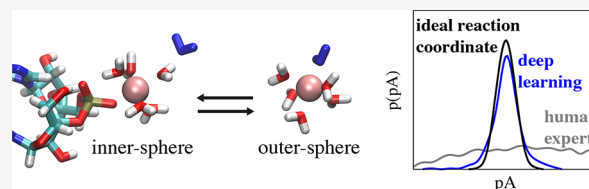


Article Recommendations



Supporting Information

ABSTRACT: Magnesium is an indispensable cofactor in countless vital processes. In order to understand its functional role, the characterization of the binding pathways to biomolecules such as RNA is crucial. Despite the importance, a molecular description is still lacking since the transition from the water-mediated outer-sphere to the direct inner-sphere coordination is on the millisecond time scale and therefore out of reach for conventional simulation techniques. To fill this gap, we use transition path sampling to resolve the binding pathways and to elucidate the role of the solvent in the binding process. The results reveal that the molecular void provoked by the leaving phosphate oxygen of the RNA is immediately filled by an entering water molecule. In addition, water molecules from the first and second hydration shell couple to the concerted exchange. To capture the intimate solute–solvent coupling, we perform a committor analysis as the basis for a machine learning algorithm that derives the optimal deep learning model from thousands of scanned architectures using hyperparameter tuning. The results reveal that the properly optimized deep network architecture recognizes the important solvent structures, extracts the relevant information, and predicts the commitment probability with high accuracy. Our results provide detailed insights into the solute–solvent coupling which is ubiquitous for kosmotropic ions and governs a large variety of biochemical reactions in aqueous solutions.



1. INTRODUCTION

Magnesium plays a vital role in almost every biological process. By now more than 800 different biochemical roles of Mg²⁺ have been identified in physiological processes ranging from the creation of cellular energy or the synthesis of biomolecules to the activation of enzymes and ribozymes.^{1–5} The specific requirement for Mg²⁺ as a cofactor is particularly pronounced in nucleic acid systems where Mg²⁺ plays structural roles by complexing negatively charged groups or catalytic roles by accelerating or inhibiting chemical reactions in ribozymes.^{3,6–8}

In RNA systems, Mg²⁺ ions are essential for two reasons: They screen the electrostatic repulsion, thus allowing RNA to fold into compact and functional structures.⁹ In addition, a smaller fraction of Mg²⁺ ions interacts directly with the functional atom groups of the RNA. These site-specific ions stabilize the three-dimensional structure further and are involved either in a direct contact (inner-sphere) or are mediated through the hydrogen bond of a coordinating water molecule (solvent-shared).^{7,9} The second reason why cations are essential is that binding of Mg²⁺ to active binding sites allows ribozymes to perform chemical reactions that would not be possible from the basic RNA building blocks alone.^{3,6}

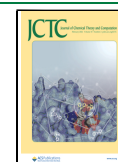
Despite the importance of Mg²⁺ in RNA biology, a detailed understanding of the Mg²⁺–RNA interactions at the atomic level is still lacking. As a first step in providing a thorough understanding, we here resolve the binding pathways of Mg²⁺ to RNA and elucidate the dynamic interplay of direct ion–RNA and indirect water-mediated interactions.

In aqueous solutions, the first hydration shell of Mg²⁺ consists of six water molecules arranged in octahedral symmetry.¹⁰ Water molecules from the first hydration shell exchange with the second, more loosely bound hydration shell on the microsecond time scale.^{11–13} This dynamic equilibrium allows for ligand exchange. Hereby, oxygen atoms are the preferred binding partners, in particular the nonbridging oxygens of the phosphate group on the backbone of RNA.^{3,14} Interestingly, water exchange around Mg²⁺ is orders of magnitude slower compared to other metal ions.^{11,15} The long lifetimes of water molecules in the first hydration shell facilitate two distinct binding arrangements: inner-sphere and outer-sphere. In inner-sphere binding, one water molecule is removed from the first hydration shell, and the ion is in direct contact with the RNA atoms. In outer-sphere binding, the interactions with the RNA are mediated by water, while Mg²⁺ remains coordinated by six water molecules.³

Does Mg²⁺ bind in inner- or outer-sphere coordination and how can it transition from the one binding mode to the other? Discerning the nature of the exact interactions is an important and controversially discussed question in the field.^{14,16,17}

Received: July 27, 2021

Published: January 27, 2022



Typically, structural knowledge on the binding mode of Mg^{2+} is obtained from crystallographic experiments. However, the correct assignment in the electron density maps remains notoriously difficult. Yet, with proper stereochemical guidelines a consistent picture emerges: Nucleobase nitrogen and carbonyls are poor inner-sphere Mg^{2+} binders,^{16,17} while the nonbridging oxygens of the phosphate group are the primary nucleic acid binding location. In large RNA structures, Mg^{2+} ions can, depending on the exact environment, bind in inner- or outer-sphere coordination,^{3,18} whereas the inner-sphere coordination is thermodynamically favored in simple mononucleotide systems.¹⁹

In addition to the structural information from crystallography, NMR can provide valuable insight into the exchange kinetics.^{11,20,21} Depending on the number of direct Mg^{2+} -RNA contacts, the time scale for ligand exchange ranges from milliseconds^{20,22,23} to hundreds of seconds.²¹ However, the structural changes at the microscopic level during an exchange process are not accessible from experiments. Here, simulations can contribute important insights by characterizing the solvent behavior and by providing a unique atomistic description of the dynamics. Yet, simulating the transition from outer-to-inner sphere binding is tremendously challenging for two reasons: According to experiments, the transition is on the millisecond to second time scale and therefore out of reach for conventional all-atom simulations. Alternatively, enhanced sampling techniques such as metadynamics, replica exchange, and umbrella sampling can be applied^{24,25} but do not provide any information on the exchange dynamics and reaction mechanism.

The second challenge is the coupling of the solvent to the exchange dynamics. Kosmotropic ions, such as Mg^{2+} , provoke strong structural ordering of the first hydration shells. Therefore, any process in aqueous solutions is expected to be governed by a complex interplay of structural, orientational, and hydrogen bonding effects extending over several hydration shells. It is therefore not surprising that the solvent not only is a spectator of the chemical process but also plays an active role in the evolution. Similarly, the dynamics of seemingly simple processes such as dipeptide isomerization, ion pair formation, water exchange between hydration shells, or proton and electron transfer is governed by solute–solvent coupling.^{26–33} Therefore, attempts in describing the dynamics of such processes in terms of simplified reaction coordinates that do not include the solute–solvent coupling are likely to fail for several reasons. (i) Solvent reorganization is orthogonal to such simplified reaction coordinates giving rise to pronounced non-Markovian behavior or memory effects.³⁴ (ii) The metastable states are not uniquely separated leading to the violation of the no-recrossing assumption and failure of transition state theory.³⁵ (iii) Enhanced sampling techniques that rely on biasing the slow degrees of freedom become inefficient as the solvent reorganization becomes slower than the reactive motion itself. Consequently, quantifying the contribution of the solvent to the reaction coordinate is one of the long-standing problems in chemical reaction kinetics.

In order to address both challenges, we apply transition path sampling as a particularly powerful sampling strategy to provide unbiased microscopic insight into the dynamics of Mg^{2+} binding to the phosphate oxygen of RNA. Subsequently, we perform a committer analysis comprising more than 28,600 configurations as the basis for a machine learning algorithm which automatically selects the optimal deep learning model

from thousands of scanned architectures in a robust and efficient manner. The resulting optimized deep neural network is shown to capture the intimate solute–solvent coupling and to provide an accurate description of the complete dynamical process.

2. METHODS

Atomistic Model and Simulation Setup. Our model system consists of an RNA dinucleotide with two guanine nucleobases (Figure 1). The RNA dinucleotide is an ideal

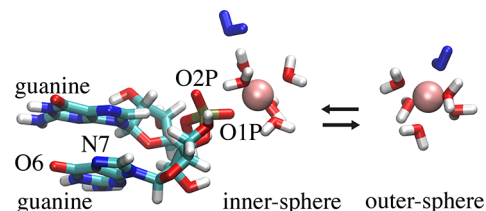


Figure 1. Simulation snapshot of the RNA dinucleotide consisting of two guanine nucleobases with a Mg^{2+} ion in inner- or outer-sphere coordination. The backbone binding sites (atoms O1P and O2P) and the N7 and the O6 binding site of guanine are shown. The exchanging water molecule is shown in blue.

model system to investigate ion-RNA interactions since it contains the three most important metal cation binding sites: The nonbridging phosphate oxygens of the backbone and the N7 and O6 metal binding site on the nucleobase.¹⁹ For Mg^{2+} , there is clear experimental evidence that the nonbridging phosphate oxygens are the primary nucleic acid binding site for Mg^{2+} .^{3,17} Since both oxygen atoms (O1P and O2P) have identical force field parameters, we focus on the interactions with O1P which has a partial charge of $-0.776e$. Our selection of the phosphate oxygens is further justified by a large number of unbiased simulations that reveal exclusive binding of Mg^{2+} to the phosphate oxygen and not to the nucleobases in agreement with previous results.²⁵ A single Mg^{2+} ion, one Cl^- ion, and 2150 water molecules are added to the cubic simulation box ($L = 40 \text{ \AA}$). Since the dinucleotide has one negative charge, the simulation box is neutral. For Mg^{2+} and Cl^- , recently optimized force field parameters were used³⁶ in combination with the TIP3P water model.³⁷ The TIP3P water model assigns partial charges of $-0.834e$ and $0.417e$ to oxygen and hydrogen. Note that to date a large variety of water models exist with some reproducing the physical properties of water better than TIP3P.³⁸ Our main motivation to use TIP3P water is that it is frequently used in biomolecular simulations since protein and nucleic acid force fields were optimized with TIP3P. The force field parameters of the RNA are taken from Amber99sb-ildn*³⁹ with parmbsc0⁴⁰ and χ_{OL3} corrections.⁴¹

The Mg^{2+} parameters were optimized in our previous work³⁶ in combination with TIP3P and are particularly suited to investigate ion binding since they reproduce experimental activity coefficients and the hydration free energy. In addition, the Mg^{2+} parameters by Mamatkulov and Schwierz³⁶ predict an interchange dissociative exchange mechanism in water in agreement with experiments, while polarizable force fields^{42–44} erroneously yield an associative mechanism.⁴⁵ Note that models with variable polarizability⁴⁶ or scaled charge force fields^{47,48} might yield improvement but are beyond the scope of our current work.

A detailed comparison of the Mamtkulov Mg^{2+} force field parameters with other parameters from the literature can be found in refs 36 and 49.

All simulations were performed using GROMACS⁵⁰ with periodic boundary conditions. Particle mesh Ewald summation was used along with a Fourier spacing of 0.12 nm and a grid interpolation up to order 4 to handle long-range electrostatic forces. Close Coulomb real space interactions were cut off at 1.2 nm, and Lennard-Jones (LJ) interactions were cut off after 1.2 nm, respectively. Long-range dispersion corrections for energy and pressure were applied to account for errors stemming from truncated LJ interactions.

The initial energy minimization was performed with the steepest descent algorithm. For each simulation, an NVT and a subsequent NPT equilibration were done for 1 ns, controlling the temperature at 300 K and at a pressure of 1 bar with the Berendsen thermostat and barostat.⁵¹ All production runs and the transition path sampling were done in the NVT ensemble at a temperature of 300 K using the velocity rescaling thermostat with stochastic term⁵² and a time step of 2 fs. Here, the velocity rescaling thermostat was used since it generates the canonical ensemble and ensures detailed balance in the canonical ensemble of transition paths.⁵³

Free Energy Profiles. The one-dimensional free energy profile as a function of the distance r_I between the Mg^{2+} ion and the oxygen atom O1P was calculated from umbrella sampling using PLUMED.⁵⁴ A force constant $k_b = 600,000$ kJ/(mol nm²) and a window spacing of 0.005 nm were used for $r_I < 0.35$ nm. A force constant $k_b = 60,000$ kJ/(mol nm²) and a window spacing of 0.01 nm were used for $r_I > 0.35$ nm. To ensure convergence, we computed the reverse pathway and performed a block analysis by dividing the 100 ns long simulation into eight individual blocks (Figure S1 in the Supporting Information.)

The two-dimensional free energy profiles as a function of r_I and the effective hydration distance s_6 were calculated from umbrella sampling using PLUMED.⁵⁴ Hereby, s_6 was defined as the sum of six Mg^{2+} -oxygen distances

$$s_6 = \sum_{i=1}^6 r_i + r_{\text{ex}} \quad (1)$$

where r_i are the distances between Mg^{2+} and the five closest water molecules, and r_{ex} is the distance between Mg^{2+} and the exchanging water molecule. A force constant $k_b = 100,000$ kJ/(mol nm²) and a window spacing of 0.01 nm were used. Without further restraints, the system shows three stable states in the two-dimensional projection (see Figure S2 in the Supporting Information). In the umbrella sampling, we focus only on transitions between the two relevant states (corresponding to the inner-sphere configuration with five coordinating water molecules and the outer-sphere coordination in which O1P is replaced by the selected water molecule for which the umbrella potential is applied). This is justified further by the results from the unbiased simulations (TPS and fleeting trajectory setup with 3.5 μs total simulation time) which clearly demonstrate that Mg^{2+} goes directly to the phosphate oxygen and never to any of the nucleobase binding sites. In the umbrella sampling, this is achieved by an additional biasing potential on the hydration number (see the Supporting Information for further details). Position restraints were applied on all heavy atoms of the dinucleotide with the exception of the nonbridging oxygen atoms of the

phosphate group. Each umbrella simulation was performed for 2 ns discarding 500 ps for equilibration. The free energy profiles were calculated using the weighted histogram analysis method (WHAM).⁵⁵

Transition State Theory. TST is the most popular theory to calculate reaction rates. In simple systems for which the reaction coordinate is exactly known, TST gives an accurate estimate of the rate. However, in complex many-body systems such as the one presented here, TST could fail due to the violation of the nonrecrossing hypothesis which forms the cornerstone of the theory. Therefore, TST can be used only to provide an upper estimate for the rate constant. For a more accurate estimate, additional corrections as implemented in the reactive flux method are required^{35,56} but are beyond the scope of our current work. Following conventional transition state theory (TST), the upper estimate of the rate constant is calculated from^{57,58}

$$k_{A \rightarrow B}^{\text{TST}} = \langle \dot{\lambda}_0 \theta(\dot{\lambda}_0) \rangle_c \frac{e^{-\beta F(\lambda^*)}}{\int_{-\infty}^{\lambda^*} d\lambda' e^{-\beta F(\lambda')}} \quad (2)$$

where λ^* is the position of the barrier top, $\theta(\dot{\lambda})$ is the Heaviside step function, and $\langle \dots \rangle_c$ denotes the average over the restrained ensemble of trajectories initiated from an equilibrium ensemble of phase points on the dividing surface.

Transition Path Sampling. Transition path sampling^{53,59} was used to harvest an ensemble of rare trajectories that connect the two stable states. Starting from an initial reactive pathway generated at high temperature, new trial trajectories were created by randomly selecting a time slice, randomizing the velocities, and integrating the equations of motion forward and backward in time. Using standard two-way shooting moves with a fixed length of 1.6 ps, trial moves are accepted if they connected the two stable states and rejected otherwise.

Committer Analysis and Transition States. For a simulation snapshot taken from a reactive transition pathway, the committer p_A is defined as the probability of the configuration initiated with randomized velocities drawn from a Maxwell–Boltzmann distribution to be committed to state A (inner-sphere coordination). Configurations from basin A have $p_A = 1$, configurations from basin B have $p_A = 0$, and transition states have $p_A = 0.5$. The commitment probability p_A was calculated from the fraction of trajectories initiated with randomized velocities that reach state A. 29,112 configurations along more than 2500 independent pathways obtained from transition path sampling were used as shooting points. 28,612 shooting points were chosen in the transition region (with $0.6 < \lambda < 1.0$ based on the coordinate λ defined in eq 7). In addition, 500 shooting points were selected in the regions of the stable states ($\lambda < 0.6$ and $\lambda > 1.0$). For each shooting point, 100 trajectories were initiated with random velocities and run forward and backward for 2 ps. A configuration was identified as a transition state if half of the trajectories relaxed into each stable state ($0.45 < p_A < 0.55$). From the ensemble of shooting point, two subsets with $r_I = 0.28 \pm 0.02$ nm or $\lambda = 0.8 \pm 0.05$ with 3,500 randomly drawn data points were selected, and the distribution $p(p_A)$ was calculated.

In total, 3.5 μs of unbiased simulation data were used to test the different putative reaction coordinates.

Commitment Probability from Deep Neural Networks. Deducing an appropriate description by visual inspection is virtually impossible if complex configurational rearrangements are considered as in the system presented here.

Neural networks, on the other hand, are particularly suited for this task. For example, in the pioneering work by Ma and Dinner,²⁸ neural networks were used to predict the committor based on a set of coordinates for the isomerization of alanine dipeptide. More recently, Jung et al. proposed and implemented a combination of path sampling and deep neural networks to guide the sampling and to extract the reaction coordinate.^{26,27,60} Following the work by Jung et al.,^{26,27} we used a deep neural network to learn the reaction coordinate from the outcome of the committor analysis by minimizing the likelihood loss function.^{61,62} Note, however, that we did not guide the sampling as described in refs 26 and 27. Instead, we performed a preceding committor analysis (as described above) and used the committor to map the molecular configurations onto the reaction coordinate $q^{\text{pred}}(\mathbf{X})$. Each configuration was described by a set of 83 physical properties (referred to as features \mathbf{X} in the following). The committor was parametrized as in refs 26 and 27

$$p_A^{\text{pred}}[q(\mathbf{X})] = (1 + e^{-q^{\text{pred}}(\mathbf{X})})^{-1} \quad (3)$$

where the predicted committor p^{pred} is a nonlinear function of all the features \mathbf{X} of the system. Note that by rescaling the reaction coordinate via $q = \tilde{q}/2$ the frequently used expression for the committor by Peters and Trout⁶² is retrieved:

$$p_A^{\text{pred}}[\tilde{q}(\mathbf{X})] = (1 + e^{-\tilde{q}^{\text{pred}}(\mathbf{X})})^{-1} = (1 + \tanh(\tilde{q}^{\text{pred}}(\mathbf{X}))/2) \quad (4)$$

Therefore, eqs 3 and 4 are expected to yield identical results. The likelihood that a model can reproduce the observed data is given by^{26,27,61,62}

$$L = \prod_{i=1}^N (p_A^{\text{pred}}([q(\mathbf{X})])^{n_A^i} (1 - p_A^{\text{pred}}([q(\mathbf{X})]))^{n_B^i}) \quad (5)$$

where N is the number of shooting points, and n_A^i and n_B^i are the number of trajectories that reach state A and B from shooting point i , respectively. Following the work by Jung et al.,^{26,27} we modeled the committor with a deep neural network. Hereby, the weight matrix that defines the connection between the nodes of the deep neural network was optimized by minimizing the negative log likelihood loss^{26,27}

$$l = -\log L(q^{\text{pred}}) = \sum_{i=1}^N (n_B^i \log(1 + e^{q^{\text{pred}}}) + n_A^i \log(1 + e^{-q^{\text{pred}}})) \quad (6)$$

The overall accuracy and generalization of the machine learning model (i.e., the deviation of the predicted values p_A^{pred} from the simulated ones p_A^{true}) was estimated by dividing the available data into a training set, a validation set, and a test set. The first was used to train the model, the second was used to validate the training result, and the third was used to check whether the final model is able to correctly predict the values for structures that were not used for training.

Training a Deep Learning Regression Model with Hyperparameter Optimization. One challenge in the application of neural networks is to choose the model architecture. As illustrated in Figure 2A, the accuracy of the network to predict the commitment probability of a configuration and to autonomously select the transition state strongly depends on the underlying model architecture. However, there is no generic way to determine all the model parameters such as the number of hidden layers, the number of

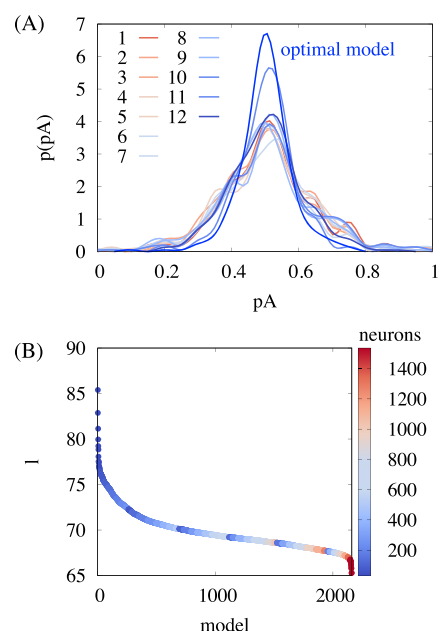


Figure 2. Dependence of the performance on the model architecture. (A) Comparison of the committor distribution $p(p_A^{\text{true}})$ for transition states selected from deep learning algorithms with different model architectures (see the Supporting Information for further details of the models). (B) Validation likelihood loss l for a random subset of model architectures. One parameter of the architecture, the total number of neurons, is shown in color. In total, several thousand different model architectures were explored by running a Keras Tuner random search in the space of model parameters.

neurons, and all hyperparameters a priori. Moreover, a network architecture that works well for one system might fail to capture other systems or dissimilar problems. Therefore, building an optimal deep neural network manually by trial and error is a time-consuming problem which highly depends on human expertise and intuition. In order to make this progress more efficient, we developed an algorithm that automatically finds the optimal network architecture. First, we specified a class of multilayer perceptron (MLP) regression models that are described by a set of hyperparameters.⁶³ Subsequently, we selected the optimal model by running a Keras Tuner random search hyperparameter optimization.⁶⁴ Hereby, the generic MLP was defined by the following set of hyperparameters: number of hidden dense layers (1–6), number of neurons per hidden layer (32–256), activation function (Rectified Linear Units (ReLU) or Scaled Exponential Linear Unit (SELU)), position of a single dropout layer (none/after feature input/middle layer/before output layer), dropout rate (0–40%), and learning rate for the Adam Optimizer (logarithmic sampling from 10^{-4} – 10^{-2}). For ReLU activation functions, a Glorot uniform initialization and a normal dropout layer were used. For SELU activation functions, a Lecun normal initialization and an alpha dropout layer were used. ReLU and SELU are the standard choices for regression models in Keras and were therefore used. The custom loss function by Jung et al.^{26,27} according to eq 6 was used. All models were trained via back-propagation using the stochastic gradient algorithm.

The data was split into a 20% test set, a 72% training set, and an 8% validation set. Different splitting of the data yielded similar results (see the Supporting Information). All features were normalized using the Keras standard scaler with mean $\mu =$

0 and standard deviation $\sigma = 1$. Each model was set up for 50 epochs with a training batch size of 128. Early stopping with patience 10 was used on the validation loss. Multiple thousand different model architectures were explored, and the likelihood loss of a random subset of 2,160 models is shown in Figure 2B.

For further optimization, a subset of best models based on minimal validation loss was chosen. The training of the best model subset was continued for up to 200 epochs with the previous batch size and early stopping. In addition, a stepwise reduction of the learning rate by a factor of 5 down to 10^{-5} was used if the validation loss reached a plateau for 7 training steps. Finally, the best model was chosen based on the highest maximum in the $p(p_A^{\text{pred}})$ distribution.

In summary, the optimization algorithm allows us to find the optimal model architecture in a quick and reliable fashion. The optimal deep learning model has five hidden layers with 256 neurons, ReLU activation, and an initial learning rate of 1.9×10^{-4} . A dropout layer with 30% dropout is placed directly before the output layer. All code was developed with Keras,⁶⁵ scikit-learn,⁶⁶ and TensorFlow.⁶⁷

Features. For each shooting point, we calculated 83 features that reflect different structural properties of the molecular configuration. Focusing only on the dominant indirect exchange, the data set has 17,477 entries. Each entry consists of 83 features, and the label p_A^{true} was calculated for each shooting point using the committor analysis. Specifically, the features include all distances r_i between Mg^{2+} and the 20 closest water molecules, distances between Mg^{2+} and different RNA atoms and the Cl^- ion, all angles a_i formed between Mg^{2+} , O1P, and the 20 closest water molecules, the Steinhardt-Nelson order parameters q_3 , q_4 , and q_6 ⁶⁸ of the first and second hydration shell, tetrahedral order parameters,⁵⁴ and the number of hydrogen bonds in the first and second hydration shell and between RNA and water (Table S1).

Transition path sampling, performed in previous work,^{31,45} yielded detailed molecular insights into the mechanism of water exchange in the first hydration shell and showed that the coordinates of the exchanging ligands need to be included to provide a reasonable description. Similarly, in the present case, a putative, knowledge-based reaction coordinate λ was defined, which combines the Mg^{2+} -RNA distance r_I and the effective hydration distance s_6 via a trigonometric function

$$\lambda = \text{atan2}(s_6 - s_6^0, r_I - r_I^0) \quad (7)$$

The atan2 function is an extension of the usual atan function with two real numbers as argument. Therewith, the atan2 function comprises enough information to yield function values in the range of $0-2\pi$ and allows us to cover all possible values for s_6 and r_I . Note that the parameters $s_6^0 = 1.18$ nm and $r_I^0 = 0.18$ nm correspond to the minima in the two-dimensional free energy profile. With this choice, $\lambda = \pi/2$ corresponds to the inner-sphere coordination, and $\lambda = 0$ corresponds to the outer-sphere coordination (Figure 3B).

Feature Relevance. To this end, the machine learning model employs a large number of features to model the reaction coordinate and to predict the commitment probability p_A^{pred} of new structures. In the following, we aim to determine the importance of each input feature. Since the deep learning network consists of a large number of nodes, weighted sums, and nonlinear transformations, the feature relevance was calculated numerically by selectively replacing single features or combinations of features by noise and resampling the model.

For the single feature relevance, we generated for every input feature i a data set in which the values \mathbf{X}_i were replaced by randomly permuted values \mathbf{X}_i^p . The random permutation approach was chosen as it exactly conserves the original distribution. The normalized relevance of the i -th feature r_s^i was defined as

$$r_s^i = r_s(\mathbf{X}_i^p) = \frac{l(\mathbf{X}_i^p) - l_{\text{opt}}}{l_{\text{max}} - l_{\text{opt}}} \quad (8)$$

where l_{opt} is the converged loss of the optimal model, and l_{max} is the largest value upon permutation. The relevance corresponds to the loss of information (i.e., the negative log likelihood increase) upon effectively removing a single feature from the data set while leaving all other features unchanged. Accordingly, the single feature rank ranges from low (unimportant) to high (important).

For single feature permutation importance, standard libraries can be used.^{66,69} For this work, we implemented a custom algorithm that extends the standard permutation importance algorithms to be able to measure the importance of combined feature sets (see below). Note that an alternative approach for the single feature analysis was proposed in ref 26 where uniform random noise was used instead of random permutations.

For the relevance of combined features, $N(N+1)/2 = 3486$ permuted data sets were generated as follows. Starting from the optimal model, the feature which yielded the smallest loss upon permutation was removed (rank 1). This feature contained the smallest amount of information and was consequently least important for the process. Maintaining the permutation of rank 1, we selected the second feature that yielded the smallest loss upon permutation (rank 2). The procedure was repeated until all features are permuted. The normalized relevance for effectively removing the information on n features is given by

$$r_c^n = r_c(\mathbf{X}_1^p, \dots, \mathbf{X}_n^p, \mathbf{X}_{n+1}, \dots, \mathbf{X}_N) = \frac{l(\mathbf{X}_1^p, \dots, \mathbf{X}_n^p, \dots, \mathbf{X}_{n+1}, \mathbf{X}_N) - l_{\text{opt}}}{l_{\text{rand}} - l_{\text{opt}}} \quad (9)$$

where l_{opt} is the converged loss of the optimal model, and l_{rand} is loss obtained by permuting all features. Here, the relevance corresponds to the increase of the negative log likelihood upon removing the combination of n features that contain the least amount of information. Accordingly, the feature combination rank ranges from low (least important combination) to high (most important combination).

3. RESULTS AND DISCUSSION

Free Energy Landscape of Mg^{2+} -RNA Interactions.

During association, one of magnesium's six strongly bound hydration waters is removed to facilitate a direct contact between Mg^{2+} and the phosphate oxygen. In the simplest case, this ligand exchange can be described by the distance r_I between Mg^{2+} and the phosphate oxygen, while all other degrees of freedom are integrated out. The corresponding one-dimensional free energy profile is shown in Figure 3A. The free energy profile has two stable states. State A corresponds to the inner-sphere coordination, and state B corresponds to the outer-sphere coordination. The free energy barrier from outer-sphere to inner-sphere is about $21 k_B T$ and exactly matches the value for water exchange.³¹ Consequently, the barrier corresponds to the free energy necessary to remove one

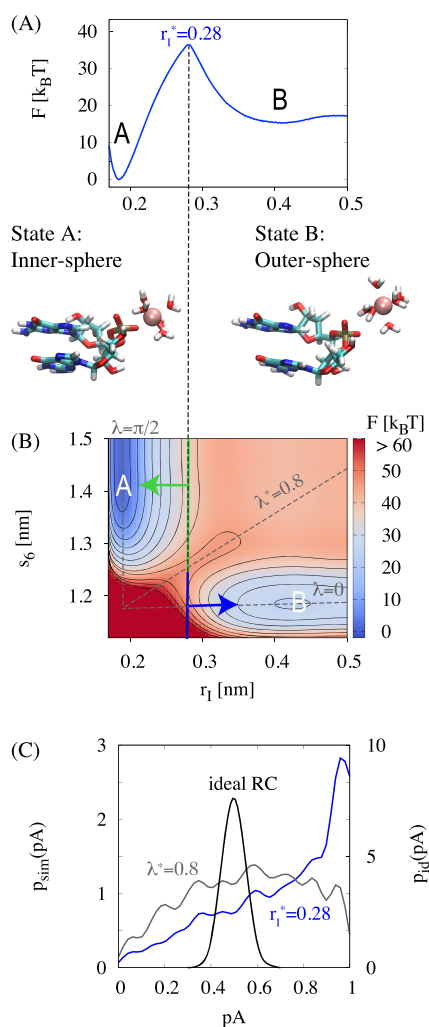


Figure 3. Free energy landscape of Mg^{2+} -RNA interactions. (A) Free energy profile $F(r_1)$ as a function of the distance between Mg^{2+} and the phosphate oxygen. Simulation snapshots of the two stable states are shown. (B) Two-dimensional free energy landscape $F(r_1, s_6)$ as a function of r_1 and s_6 where s_6 is the sum over the distances between Mg^{2+} and the five closest molecules and the exchanging water molecule. The dashed line indicates configurations from the top of the free energy profile with $r_1^* = 0.28$ nm shown in (A). Trajectories, initiated from the upper green stripe, relax back into state A, and trajectories from the lower blue stripe relax back into state B. The diagonal dashed line for $\lambda^* = 0.8$ approximates the saddle between states A and B. (C) Committor distributions $p_{\text{Sim}}(p_A)$ for trajectories initiated with $r_1^* = 0.28$ nm (top of the one-dimensional free energy profile shown in A) and with $\lambda^* = 0.8$ (saddle of two-dimensional free energy profile shown in B). $p_{\text{id}}(p_A)$ is the distribution expected for an ideal reaction coordinate with 3500 shooting points.

water molecule from the first hydration shell in order to facilitate a direct contact with the phosphate oxygen. The inner-sphere coordination is thermodynamically more stable in agreement with experimental findings¹⁹ and Collins' empirical rule like-seeks-like.⁷⁰ Due to the high charge density of the phosphate oxygens, direct ion pairing with a high binding affinity is expected.

Using transition state theory TST (eq 2), we can provide an upper estimate of the exchange rate or conversely a lower estimate of the lifetime. Here, it is essential to mention that the true rate could be significantly smaller due to the violation of the nonrecrossing hypothesis. As a lower limit, Mg^{2+} is

estimated to remain about 300 s in the inner-sphere coordination before transitioning to outer-sphere. Similarly, Mg^{2+} is estimated to remain about 0.2 ms in the outer-sphere coordination before transitioning back to inner-sphere. Note that the exchange between the outer-sphere coordination and bulk is much faster since the free energy barrier is significantly smaller (Figure 3A). The lifetime of the outer-sphere coordination is in agreement with the millisecond time scale observed experimentally.^{20,22,23} On the other hand, the computed lifetime of the inner-sphere coordination is likely too high reflecting the shortcoming of current Mg^{2+} force fields in reproducing experimental binding affinities at nucleic acid binding sites.^{28,49,71}

The quality of a reaction coordinate can be assessed by a committor analysis. For an ideal reaction coordinate, about half of the trajectories initiated from the barrier top are expected to relax back to either stable state. Consequently, the distribution $p(p_A)$ of the probability to relax back to state A should have a sharp peak at $p_A \approx 1/2$ (binomial committor distribution). While r_1 provides a simplified description of the process, it is not an adequate reaction coordinate by itself. The committor analysis (Figure 3C) shows that most configurations, initiated with $r_1 = 0.28$ nm, relax back to the inner-sphere coordination. Therefore, the Mg^{2+} -oxygen distance alone is insufficient to describe the dynamics of the transition. To provide a more realistic picture, the water molecules from the first hydration shells have to be included. Figure 3B shows the two-dimensional free energy landscape as a function of r_1 and the hydration parameter s_6 , which includes the distances of the five closest waters and the exchanging water (eq 1). From the two-dimensional representation, the failure of r_1 as the reaction coordinate can be rationalized: Trajectories starting from the upper panel ($s_6 > 1.24$ nm) are committed to state A, while trajectories starting from the lower panel ($s_6 < 1.24$ nm) are committed to state B. r_1 and s_6 can be combined into a putative, knowledge-based reaction coordinate λ (eq 7). Based on the committor distribution (Figure 3C), λ provides significant improvement compared to r_1 . Still, configurations with $\lambda^* = 0.8$ lead to a much broader distribution compared to the ideal binomial distribution.

These results show that free energy profiles along a few simple coordinates provide valuable initial insight. Yet, the committor analysis reveals that the exchange dynamics is more complex than the free energy profiles might suggest.

Kinetic Pathways from Transition Path Sampling. To gain insight into the kinetic pathways of Mg^{2+} association and dissociation, transition path sampling is applied to sample a large number of inner-to-outer sphere transitions. Four representative transition paths that connect the two stable states are shown in Figure 4A. Figure 4C shows the distribution of transition times. Typically, the exchanging water molecules spend less than 0.5 ps in transition. This time is considerably smaller compared to the millisecond time scale of the stable states. The clear separation of time scales highlights the path sampling method as a particularly powerful sampling strategy for these systems.

The distribution of the exchange angles (Figure 4B) along reactive pathways indicates that two alternative exchange pathways exist: In the *indirect exchange mechanism*, the leaving oxygen ligand and the entering water molecule occupy different positions on the water octahedron (Figure 4D). During activation, one water molecule from the second hydration shell enters the molecular void between the

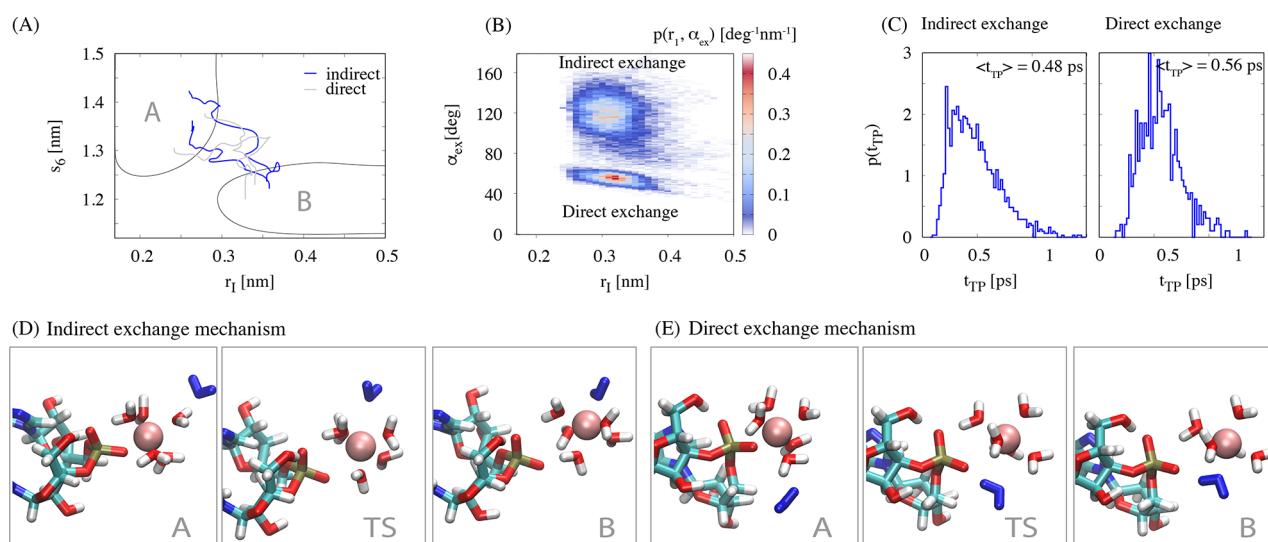


Figure 4. Kinetic pathways from transition path sampling. (A) Four representative pathways connecting the two stable states. Blue/gray pathways correspond to the indirect/direct exchange mechanism. (B) Probability distribution along transition pathways for the distance r_l between Mg^{2+} and the phosphate oxygen and the exchange angle α_{ex} between phosphate oxygen, Mg^{2+} , and exchanging water oxygen. (C) Distribution of transition times for the indirect and the direct exchange mechanisms. (D) Indirect Mg^{2+} exchange mechanism in which the leaving phosphate oxygen and the incoming water molecule occupy different positions on the water octahedron. (E) Direct Mg^{2+} exchange mechanism in which the leaving phosphate oxygen and the incoming water molecule occupy the same position on the water octahedron. In (D) and (E), the five closest water molecules are shown. The incoming water molecule is highlighted in blue.

Table 1. Properties of the Transition State Ensemble^a

mechanism	r_l [Å]	r_{ex} [Å]	r_s [Å]	α_{ex} [deg]	τ [ps]
indirect	3.17 ± 0.03	3.51 ± 0.03	1.928 ± 0.003	122.9 ± 14.7	0.48 ± 0.01
direct	3.28 ± 0.03	3.46 ± 0.03	1.928 ± 0.003	47.7 ± 5.1	0.56 ± 0.01

^a Mg^{2+} -O1P distance r_l , Mg^{2+} -oxygen distance of exchanging water r_{ex} , Mg^{2+} -oxygen distance of the five closest water molecules r_s , angle between O1P, Mg^{2+} , and the exchanging water molecule α_{ex} , average transition time τ . Standard deviations are indicated. A sample size of 1759 or 754 transition states was used for the indirect and direct exchange mechanisms, respectively.

hydration shells. This motion leads to a concerted motion of the phosphate oxygen out of the first hydration shell. The distances of the leaving phosphate oxygen and the entering water are elongated compared to their equilibrium values (Table 1). Reflecting balanced electrostatic interactions, the Mg^{2+} -phosphate oxygen distance is smaller than the Mg^{2+} -water oxygen distance due to the smaller partial charge on the phosphate oxygen compared to the water oxygen. The distances of the five closest molecules remain relatively unchanged (Table 1). Yet, they rearrange such that the transition state has an approximate mirror symmetry. The mirror plane is perpendicular to the plane composed of Mg^{2+} , the phosphate, and water oxygen and contains three water molecules (Figure 4D).

In the *direct exchange mechanism*, the leaving oxygen ligand and the entering water molecule occupy the same positions on the water octahedron (Figure 4E). The exchange arises via the attack of the incoming water onto the edge of the octahedron formed by the oxygen ligands. Similar as in the indirect pathway, the Mg^{2+} -phosphate oxygen distance is slightly smaller than the Mg^{2+} -water oxygen distance, while the distances of the five closest water molecules remain relatively unchanged (Table 1). In the transition state, the five closest water molecules form a square pyramidal coordination, and the transition state has a distorted C_2 symmetry (Figure 4E).

Based on the change of bond length during activation, both pathways correspond to an interchange dissociative (I_d) process and are akin to the pathways of water exchange.³¹ In

equilibrium, the indirect exchange is observed much more frequently (92%) compared to the direct mechanism (8%) since configurations with cis positions of exchanging ligands (direct pathways) are energetically less favorable compared to trans positions (indirect pathways).⁷²

The results reveal that phosphate oxygen, exchanging water, and the five closest water molecules play a decisive role in the exchange mechanism. However, additional simulations in which those coordinates were fixed, while the solvent outside the first hydration shell was relaxed, show that they are yet insufficient to predict p_A . Consequently, solvent molecules beyond the first hydration shell are crucial for the exchange and need to be considered explicitly.

Optimized Deep Neural Networks for Quantitative Predictions. During the transition from outer-to-inner sphere binding, water molecules from the first two hydration shells couple to the exchange. The reordering of close and distant water molecules determines whether the process can proceed or not. This behavior might be expected since the kosmotropic Mg^{2+} ion causes strong orientational ordering in the first hydration shells leading to long-range and collective interactions. However, resolving the subtle rearrangements and providing a quantitative description of the solute–solvent coupling is a demanding problem that is impossible to solve by visual inspection. In order to make progress in quantifying the solvent participation, we use a deep neural network to model the outer-to-inner sphere exchange. Here, we focus the machine learning on the dominant indirect exchange. In

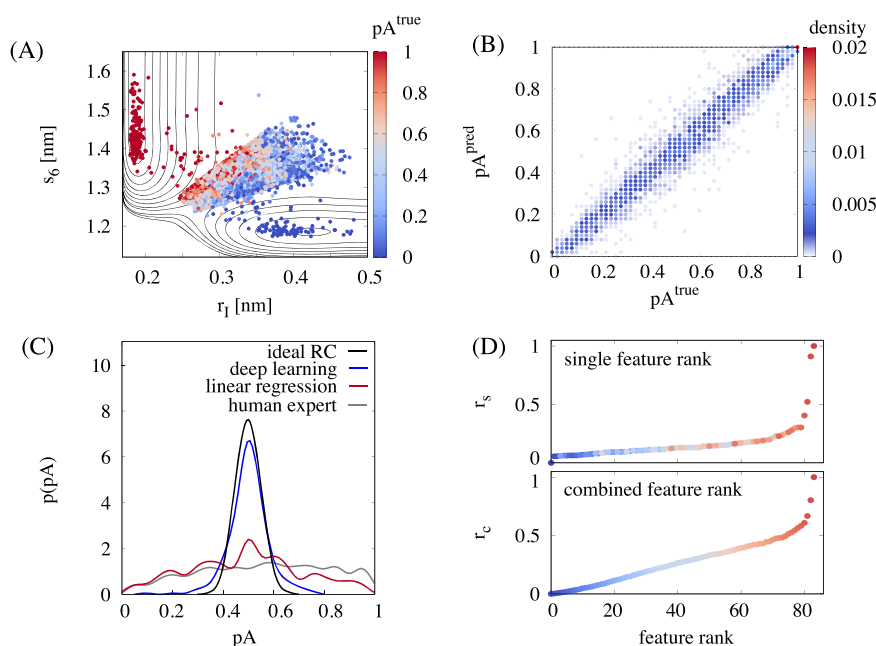


Figure 5. Reaction coordinate from artificial intelligence. (A) Data set used for machine learning. The committor probability p_A^{true} and free energy contour are shown as a function of the features r_1 and s_6 for the full data set consisting of 17,477 entries for indirect exchange pathways (72% training set, 8% validation set, 20% test set). (B) Committor values p_A^{pred} predicted by the optimized deep neural network correlated with the values p_A^{true} obtained from the committor simulations. The RMS error of the prediction is 6.5%. (C) Comparison of the committor distribution $p(p_A)$ for transition states selected from the deep learning algorithm, from linear regression over all features, and from the expert knowledge using eq 7 and the binomial distribution expected for an ideal reaction coordinate.⁶¹ (D) Ranking of the features according to their relevance in the machine learned reaction coordinate: single feature relevance r_s (top) and combined feature relevance r_c (bottom). The color indicates the rank of the features according to the combined feature relevance. The corresponding features are shown in Table 2 and Table S2.

particular, we use 17,477 structures along independent transition paths and their commitment probabilities p_A (Figure 5A) to learn the functional relation between p_A and the features describing the structure of Mg^{2+} , RNA, and the first two hydration shells.

The choice of the architecture of the deep learning model is essential for its performance. To derive the optimal deep learning model, we have defined an algorithm that systematically selects the optimal architecture by scanning through thousands of individual models using hyperparameter optimization. In order to make robust predictions and prevent overfitting, we optimize the neural network on the training set and select the model that performs best on the validation set. Finally, using the test set, we illustrate the performance of the optimal machine learning model in predicting the commitment probability of unknown structures (Figure 5B). The results demonstrate that the optimized deep neural network is capable of predicting p_A with an RMS error of 6.5%. The high accuracy in predicting the progress of the binding process clearly shows that the network extracts all relevant information, combines it in a weighted nonlinear fashion to a scalar reaction coordinate, and captures the details of the solute–solvent coupling precisely.

Further insight into the quality of the predictions is obtained from the distribution of commitment probability $p(p_A)$ of the transition states selected autonomously by the neural network (Figure 5C). The distribution is unimodal and sharply peaked at $p_A \approx 0.5$ and closely resembles the binomial distribution expected for an ideal reaction coordinate.⁶¹ Consequently, the information contained in the features is sufficient for the network to single out the transition state. The results from deep learning provide significant improvement compared to

the reaction coordinate based on expert knowledge and highlight the machine learning ansatz as a particularly useful strategy in recognizing the relevant patterns. In addition, the results from deep learning outperform the results from linear regression based on the exact same features (Figure 5C). Therefore, hidden layers and a nonlinear combination of features using activation functions are essential to describe the many-body interactions. At the same time, the complexity of the deep learning model prohibits further insight into the reaction mechanism. In this regard, it is particularly useful to evaluate the contribution of each feature. Two complementary rankings are presented in Figure 5D. The single feature ranking quantifies the relevance of a single feature independent of all others. Since the single feature ranking can contain redundant information, the complementary combined feature rank is given, which yields the most relevant combination of features. Taken together, a consistent picture emerges: All features describing the molecular structure within the first two hydration shells contain information that is relevant for the process. Adding this information to the model leads to a continuous decrease of the likelihood loss and therefore to a linear increase of the relevance r_c . Finally, four features give rise to an exponential increase in the relevance and carry about 40% of the information (Table 2). These features reflect the concerted motion of the leaving phosphate oxygen and the entering water molecule as well as the rearrangement of the five closest water molecules from octahedral to mirror symmetry. At the same time, the remaining 60% of the information is distributed over the remaining 79 features reflecting the importance and many-body nature of the solvent–solute coupling.

Table 2. Ranking of the Eight Most Important Features in the Machine Learned Reaction Coordinate According to Their Normalized Relevance (Eqs 8 and 9)^a

c-rank	feature	s-rank	feature
84	$r_I - r_{ex}$	84	$r_I - r_{ex}$
83	r_I	83	r_I
82	q_{40}	82	q_{40}
81	r_P	81	r_P
80	h_{OIP}^1	80	h_{ex}^1
79	h_{ex}^1	79	q_{41}
78	a_1	78	r_{Cl}
77	s_6	77	a_7

^aThe combined feature rank (c-rank) corresponds to the combination of $N - n$ features that contains the most information, i.e., yields the smallest log likelihood loss upon permuting n features. The single feature rank (s-rank) corresponds to the feature which yields the highest loss upon permuting the feature while leaving all other features unchanged. The ranking of all $N = 83$ features is given in Table S1.

4. CONCLUSION

Characterizing the kinetic pathways of Mg^{2+} binding to biomolecules such as RNA is fundamental in understanding its functional role in biochemical processes. Yet, the transition from water-mediated outer-sphere to direct inner-sphere binding is on the millisecond time scale and therefore out of reach for conventional all-atom simulations. To fill this gap, we used transition path sampling to resolve the kinetic pathways of Mg^{2+} binding to the most important ion binding site on RNA, namely the phosphate oxygen. The results reveal a superior indirect pathway and an inferior direct exchange pathway. In both pathways, the molecular void in the first hydration shell provoked by the leaving phosphate oxygen is immediately filled by an entering water. At the same time, the water molecules from the first and second hydration shell couple to the concerted exchange. These long-range and collective interactions are a direct consequence of the high ionic charge density of Mg^{2+} which provokes strong ordering in the surrounding solvent and an intimate coupling between solute and solvent. Consequently, ligand exchange gives rise to a complex interplay of orientational, packing, and hydrogen bonding effects in which the collective reorientation and translation of several solvent molecules become important.

A complete understanding of the dynamics requires knowledge of the detailed molecular motions involved in the exchange process. However, quantifying their contribution is exceptionally difficult. Instantaneous fluctuations, resulting from different solvent configurations, influence the progress in particular since the time scale of solvent reorientation (about 10 ps) is slower than the reactive motion itself (0.4 ps). In order to quantify how the reactant and solvent dynamics are coupled, the rapidly growing field of machine learning offers exciting possibilities in extracting complex patterns in large data sets and in finding optimal reaction coordinates.^{26–28,60,73,74} The results presented here reveal that a properly optimized deep neural network is particularly suited to recognize the molecular motions that occur during the course of the binding, to extract the relevant information, and to predict the commitment probability with high accuracy. About half of the information on the dynamics is contained in the concerted motion of the leaving phosphate oxygen and the entering water molecule as well as in the rearrangement of the

five closest water molecules. The other half is contained in the solvent structure rendering deep neural networks particularly useful in recognizing the relevant molecular structures.

The question how the solvent affects processes in aqueous solutions is ubiquitous in all areas of chemistry and biology. Here, machine learning provides a promising perspective to explore the intimate coupling between charged solutes and the solvent at the molecular level.^{26,27,73} Still, more work is required to investigate whether a simple one-dimensional reaction coordinate exists that captures such complex dynamics.⁷⁵

■ ASSOCIATED CONTENT

Supporting Information

The Supporting Information is available free of charge at <https://pubs.acs.org/doi/10.1021/acs.jctc.1c00752>.

Further discussion of two-dimensional free energy landscape, commitment probability from constrained simulations, feature definition, and feature ranking (PDF)

■ AUTHOR INFORMATION

Corresponding Author

Nadine Schwierz – Department of Theoretical Biophysics, Max-Planck-Institute of Biophysics, 60438 Frankfurt am Main, Germany; orcid.org/0000-0003-4191-2674; Email: Nadine.Schwierz@biophys.mpg.de

Author

Jan Neumann – Allianz Global Investors GmbH, 60323 Frankfurt am Main, Germany

Complete contact information is available at: <https://pubs.acs.org/doi/10.1021/acs.jctc.1c00752>

Funding

Open access funded by Max Planck Society.

Notes

The authors declare no competing financial interest.

■ ACKNOWLEDGMENTS

This work was funded by the Deutsche Forschungsgemeinschaft (DFG, German Research Foundation), Emmy Noether program, Grant No. 315221747. LOEWE CSC and GOETHE HLR are acknowledged for supercomputing access. N.S. thanks Roland K. O. Sigel and Harald Schwalbe for inspiring discussions on metal ion binding. N.S. also thanks Phill L. Geissler and Marieke Schor for helpful discussions on transition path sampling. In addition, N.S. thanks Hendrik Jung and Roberto Covino for fruitful discussions and for comments on the manuscript. Most importantly, we thank Gerhard Hummer for introducing us to the combination of path sampling and machine learning and for providing critical comments on the manuscript and stimulating discussions.

■ REFERENCES

- (1) Williams, N. H. Magnesium Ion Catalyzed ATP Hydrolysis. *J. Am. Chem. Soc.* **2000**, *122*, 12023–12024.
- (2) Terasaki, M.; Rubin, H. Evidence that intracellular magnesium is present in cells at a regulatory concentration for protein synthesis. *Proc. Natl. Acad. Sci. U.S.A.* **1985**, *82*, 7324–7326.
- (3) Pyle, A. Metal ions in the structure and function of RNA. *J. Biol. Inorg. Chem.* **2002**, *7*, 679–690.

- (4) Black, C. B.; Huang, H. W.; Cowan, J. A. Biological coordination chemistry of magnesium, sodium, and potassium ions. Protein and nucleotide binding sites. *Coordin. Chem. Rev.* **1994**, *135*–136, 165–202.
- (5) Weston, J. *Biochemistry of Magnesium*, 4th ed.; John Wiley & Sons, Ltd.: Chichester, UK, 2009; Vol. 15.
- (6) Woodson, S. A. Metal ions and RNA folding: a highly charged topic with a dynamic future. *Curr. Opin. Chem. Biol.* **2005**, *9*, 104–109.
- (7) Misra, V. K.; Draper, D. E. The Linkage between Magnesium Binding and RNA Folding. *J. Mol. Biol.* **2002**, *317*, 507–521.
- (8) Schnabl, J.; Sigel, R. K. Controlling ribozyme activity by metal ions. *Curr. Opin. Chem. Biol.* **2010**, *14*, 269–275.
- (9) Lipfert, J.; Doniach, S.; Das, R.; Herschlag, D. Understanding nucleic acid-ion interactions. *Annu. Rev. Biochem.* **2014**, *83*, 813–841.
- (10) Marcus, Y. Ionic Radii in Aqueous Solutions. *Chem. Rev.* **1988**, *88*, 1475–1498.
- (11) Helm, L.; Merbach, A. E. Water exchange on metal ions: experiments and simulations. *Coordin. Chem. Rev.* **1999**, *187*, 151–181.
- (12) Neely, J.; Connick, R. Rate of Water Exchange from Hydrated Magnesium Ion. *J. Am. Chem. Soc.* **1970**, *92*, 3476–3478.
- (13) Bleuzen, A.; Pittet, P. A.; Helm, L.; Merbach, A. E. Water Exchange on Magnesium(II) in Aqueous Solution: a Variable Temperature and Pressure. *Magn. Reson. Chem.* **1997**, *35*, 765–773.
- (14) Auffinger, P.; Westhof, E.; Grover, N. Metal Ion Binding to RNA. *Met Ions Life Sci.* **2011**, *9*, 1–35.
- (15) Lee, Y.; Thirumalai, D.; Hyeon, C. Ultrasensitivity of Water Exchange Kinetics to the Size of Metal Ion. *J. Am. Chem. Soc.* **2017**, *139*, 12334–12337.
- (16) Leonarski, F.; D'Ascenzo, L.; Auffinger, P. Nucleobase carbonyl groups are poor Mg^{2+} inner-sphere binders but excellent monovalent ion binders—a critical PDB survey. *RNA* **2019**, *25*, 173–192.
- (17) Leonarski, F.; D'Ascenzo, L.; Auffinger, P. Mg^{2+} ions: do they bind to nucleobase nitrogens? *Nucleic Acids Res.* **2017**, *45*, 987–1004.
- (18) Nguyen, H. T.; Thirumalai, D. Charge Density of Cation Determines Inner versus Outer Shell Coordination to Phosphate in RNA. *J. Phys. Chem. B* **2020**, *124*, 4114–4122.
- (19) Sigel, R. K.; Sigel, H. A stability concept for metal ion coordination to single-stranded nucleic acids and affinities of individual sites. *Acc. Chem. Res.* **2010**, *43*, 974–984.
- (20) Szabó, Z. Multinuclear NMR studies of the interaction of metal ions with adenine-nucleotides. *Coordin. Chem. Rev.* **2008**, *252*, 2362–2380.
- (21) Kowerko, D.; König, S. L. B.; Skilandat, M.; Kruschel, D.; Hadzic, M. C. A. S.; Cardo, L.; Sigel, R. K. O. Cation-induced kinetic heterogeneity of the intron–exon recognition in single group II introns. *Proc. Natl. Acad. Sci. U.S.A.* **2015**, *112*, 3403–3408.
- (22) Freisinger, E.; Sigel, R. K. O. From nucleotides to ribozymes—A comparison of their metal ion binding properties. *Coordin. Chem. Rev.* **2007**, *251*, 1834–1851.
- (23) Cowan, J. A. Coordination chemistry of magnesium ions and 5S rRNA (*Escherichia coli*): binding parameters, ligand symmetry, and implications for activity. *J. Am. Chem. Soc.* **2015**, *113*, 675–676.
- (24) Cunha, R. A.; Bussi, G. Unraveling Mg^{2+} –RNA binding with atomistic molecular dynamics. *RNA* **2017**, *23*, 628–638.
- (25) Schwierz, N.; Cruz-León, S. Hofmeister Series for Metal-Cation–RNA Interactions: The Interplay of Binding Affinity and Exchange Kinetics. *Langmuir* **2020**, *36*, 5979–5989.
- (26) Jung, H.; Covino, R.; Hummer, G. Artificial Intelligence Assists Discovery of Reaction Coordinates and Mechanisms from Molecular Dynamics Simulations. *arXiv:1901.04595*. 2019. <https://arxiv.org/abs/1901.04595> (accessed 2022-01-26).
- (27) Jung, H.; Covino, R.; Arjun, A.; Bolhuis, P. G.; Hummer, G. Autonomous artificial intelligence discovers mechanisms of molecular self-organization in virtual experiments. *arXiv:2105.06673*. 2021. <https://arxiv.org/abs/2105.06673> (accessed 2022-01-26).
- (28) Ma, A.; Dinner, A. R. Automatic Method for Identifying Reaction Coordinates in Complex Systems. *J. Phys. Chem. B* **2005**, *109*, 6769–6779.
- (29) Geissler, P. L.; Dellago, C.; Chandler, D. Kinetic Pathways of Ion Pair Dissociation in Water. *J. Phys. Chem. B* **1999**, *103*, 3706–3710.
- (30) Ballard, A. J.; Dellago, C. Toward the Mechanism of Ionic Dissociation in Water. *J. Phys. Chem. B* **2012**, *116*, 13490–13497.
- (31) Schwierz, N. Kinetic pathways of water exchange in the first hydration shell of magnesium. *J. Chem. Phys.* **2020**, *152*, 224106.
- (32) Geissler, P. L.; Dellago, C.; Chandler, D.; Hutter, J.; Parrinello, M. Autoionization in liquid water. *Science* **2001**, *291*, 2121–2124.
- (33) Rossky, P. J.; Simon, J. D. Dynamics of chemical processes in polar solvents. *Nature* **1994**, *370*, 263–269.
- (34) Kappler, J.; Daldrop, J. O.; Brünig, F. N.; Boehle, M. D.; Netz, R. R. Memory-induced acceleration and slowdown of barrier crossing. *J. Chem. Phys.* **2018**, *148*, 014903–13.
- (35) Bolhuis, P. G.; Dellago, C. In *Reviews in Computational Chemistry*; Lipkowitz, K. B., Ed.; Trajectory-Based Rare Events Simulations; Vol. 27, DOI: 10.1002/9780470890905.ch3.
- (36) Mamatkulov, S.; Schwierz, N. Force fields for monovalent and divalent metal cations in TIP3P water based on thermodynamic and kinetic properties. *J. Chem. Phys.* **2018**, *148*, 074504.
- (37) Jorgensen, W. L.; Chandrasekhar, J.; Madura, J. D.; Impey, R. W.; Klein, M. L. Comparison of simple potential functions for simulating liquid water. *J. Chem. Phys.* **1983**, *79*, 926–935.
- (38) Vega, C.; Abascal, J. L. F. Simulating water with rigid non-polarizable models: a general perspective. *Phys. Chem. Chem. Phys.* **2011**, *13*, 19663–27.
- (39) Cornell, W. D.; Cieplak, P.; Bayly, C. I.; Gould, I. R.; Merz, K. M.; Ferguson, D. M.; Spellmeyer, D. C.; Fox, T.; Caldwell, J. W.; Kollman, P. A. A second generation force field for the simulation of proteins, nucleic acids, and organic molecules. *J. Am. Chem. Soc.* **1995**, *117*, 5179–5197.
- (40) Pérez, A.; Marchán, I.; Svozil, D.; Spöner, J.; Cheatham, T. E.; Lauthon, C. A.; Orozco, M. Refinement of the AMBER Force Field for Nucleic Acids: Improving the Description of α/γ Conformers. *Biophys. J.* **2007**, *92*, 3817–3829.
- (41) Zgarbova, M.; Otyepka, M.; Spöner, J.; Mladek, A.; Banas, P.; Cheatham, T. E.; Jurecka, P. Refinement of the Cornell et al. Nucleic Acids Force Field Based on Reference Quantum Chemical Calculations of Glycosidic Torsion Profiles. *J. Chem. Theory Comput.* **2011**, *7*, 2886–2902.
- (42) Jiao, D.; King, C.; Grossfield, A.; Darden, T. A.; Ren, P. Simulation of Ca^{2+} and Mg^{2+} Solvation Using Polarizable Atomic Multipole Potential. *J. Phys. Chem. B* **2006**, *110*, 18553–18559.
- (43) Wu, J. C.; Piquemal, J.-P.; Chaudret, R.; Reinhardt, P.; Ren, P. Polarizable Molecular Dynamics Simulation of Zn(II) in Water Using the AMOEBA Force Field. *J. Chem. Theory Comput.* **2010**, *6*, 2059–2070.
- (44) Ponder, J. W.; Wu, C.; Ren, P.; Pande, V. S.; Chodera, J. D.; Schnieders, M. J.; Haque, I.; Mobley, D. L.; Lambrecht, D. S.; DiStasio, R. A.; Head-Gordon, M.; Clark, G. N. I.; Johnson, M. E.; Head-Gordon, T. Current Status of the AMOEBA Polarizable Force Field. *J. Phys. Chem. B* **2010**, *114*, 2549–2564.
- (45) Falkner, S.; Schwierz, N. Kinetic pathways of water exchange in the first hydration shell of magnesium: Influence of water model and ionic force field. *J. Chem. Phys.* **2021**, *155*, 084503.
- (46) Kurnikov, I. V.; Kurnikova, M. Modeling Electronic Polarizability Changes in the Course of a Magnesium Ion Water Ligand Exchange Process. *J. Phys. Chem. B* **2015**, *119*, 10275–10286.
- (47) Zeron, I. M.; Abascal, J. L. F.; Vega, C. A force field of Li^+ , Na^+ , K^+ , Mg^{2+} , Ca^{2+} , Cl^- , and SO_4^{2-} in aqueous solution based on the TIP4P/2005 water model and scaled charges for the ions. *J. Chem. Phys.* **2019**, *151*, 134504.
- (48) Zeron, I. M.; Gonzalez, M. A.; Errani, E.; Vega, C.; Abascal, J. L. F. In Silico Seawater. *J. Chem. Theory Comput.* **2021**, *17*, 1715–1725.

- (49) Grotz, K. K.; Cruz-León, S.; Schwierz, N. Optimized Magnesium Force Field Parameters for Biomolecular Simulations with Accurate Solvation, Ion-Binding, and Water-Exchange Properties. *J. Chem. Theory Comput.* **2021**, *17*, 2530–2540.
- (50) Hess, B.; Kutzner, C.; Van Der Spoel, D.; Lindahl, E. GROMACS 4: algorithms for highly efficient, load-balanced, and scalable molecular simulation. *J. Chem. Theory Comput.* **2008**, *4*, 435–447.
- (51) Berendsen, H. J.; Postma, J. v.; van Gunsteren, W. F.; DiNola, A.; Haak, J. Molecular dynamics with coupling to an external bath. *J. Chem. Phys.* **1984**, *81*, 3684–3690.
- (52) Bussi, G.; Donadio, D.; Parrinello, M. Canonical sampling through velocity rescaling. *J. Chem. Phys.* **2007**, *126*, 014101.
- (53) Bolhuis, P. G.; Chandler, D.; Dellago, C.; Geissler, P. L. Transition Path Sampling: Throwing Ropes Over Rough Mountain Passes, in the Dark. *Annu. Rev. Phys. Chem.* **2002**, *53*, 291–318.
- (54) Tribello, G. A.; Bonomi, M.; Branduardi, D.; Camilloni, C.; Bussi, G. PLUMED 2: New feathers for an old bird. *Comput. Phys. Commun.* **2014**, *185*, 604–613.
- (55) Kumar, S.; Bouzida, D.; Swendsen, R. H.; Kollman, P. A.; Rosenberg, J. M. The weighted histogram analysis method for free-energy calculations on biomolecules. I. The method. *J. Comput. Chem.* **1992**, *13*, 1011–1021.
- (56) Chandler, D. Statistical mechanics of isomerization dynamics in liquids and the transition state approximation. *J. Chem. Phys.* **1978**, *68*, 2959–13.
- (57) Eyring, H. The Activated Complex in Chemical Reactions. *J. Chem. Phys.* **1935**, *3*, 107–115.
- (58) Wigner, E. The transition state method. *Trans. Faraday Soc.* **1938**, *34*, 29–13.
- (59) Dellago, C.; Bolhuis, P. G.; Csajka, F. S.; Chandler, D. Transition path sampling and the calculation of rate constants. *J. Chem. Phys.* **1998**, *108*, 1964–1977.
- (60) Jung, H.; Okazaki, K.-i.; Hummer, G. Transition path sampling of rare events by shooting from the top. *J. Chem. Phys.* **2017**, *147*, 152716–11.
- (61) Peters, B.; Trout, B. L. Obtaining reaction coordinates by likelihood maximization. *J. Chem. Phys.* **2006**, *125*, 054108.
- (62) Peters, B.; Beckham, G. T.; Trout, B. L. Extensions to the likelihood maximization approach for finding reaction coordinates. *J. Chem. Phys.* **2007**, *127*, 034109–10.
- (63) Géron, A. *Hands-On Machine Learning with Scikit-Learn, Keras, and TensorFlow*, 2nd ed.; O'Reilly Media: 2019.
- (64) O'Malley, T.; Bursztein, E.; Long, J.; Chollet, F.; Jin, H.; Invernizzi, L. Keras Tuner. 2020. <https://github.com/keras-team/keras-tuner> (accessed 2022-01-26).
- (65) Chollet, F. keras. 2015. <https://github.com/fchollet/keras> (accessed 2022-01-26).
- (66) Pedregosa, F.; Varoquaux, G.; Gramfort, A.; Michel, V.; Thirion, B.; Grisel, O.; Blondel, M.; Prettenhofer, P.; Weiss, R.; Dubourg, V.; Vanderplas, J.; Passos, A.; Cournapeau, D.; Brucher, M.; Perrot, M.; Duchesnay, E. Scikit-learn: Machine Learning in Python. *Journal of Machine Learning Research* **2011**, *12*, 2825–2830.
- (67) Abadi, M.; Agarwal, A.; Barham, P.; Brevdo, E.; Chen, Z.; Citro, C.; Corrado, G. S.; Davis, A.; Dean, J.; Devin, M.; Ghemawat, S.; Goodfellow, I.; Harp, A.; Irving, G.; Isard, M.; Jia, Y.; Jozefowicz, R.; Kaiser, L.; Kudlur, M.; Levenberg, J.; Mané, D.; Monga, R.; Moore, S.; Murray, D.; Olah, C.; Schuster, M.; Shlens, J.; Steiner, B.; Sutskever, I.; Talwar, K.; Tucker, P.; Vanhoucke, V.; Vasudevan, V.; Viégas, F.; Vinyals, O.; Warden, P.; Wattenberg, M.; Wicke, M.; Yu, Y.; Zheng, X. TensorFlow: Large-Scale Machine Learning on Heterogeneous Systems. 2015. <http://tensorflow.org/> (accessed 2022-01-26). Software available from [tensorflow.org](https://www.tensorflow.org/).
- (68) Steinhardt, P. J.; Nelson, D. R.; Ronchetti, M. Bond-orientational order in liquids and glasses. *Phys. Rev. B* **1983**, *28*, 784–805.
- (69) Korobov, M. Permutation Importance. 2017. <https://github.com/eli5-org/eli5> (accessed 2022-01-26).
- (70) Collins, K. D. Ions from the Hofmeister series and osmolytes: effects on proteins in solution and in the crystallization process. *Methods* **2004**, *34*, 300–311.
- (71) Cruz-León, S.; Grotz, K. K.; Schwierz, N. Extended magnesium and calcium force field parameters for accurate ion-nucleic acid interactions in biomolecular simulations. *J. Chem. Phys.* **2021**, *154*, 171102.
- (72) Rotzinger, F. P. Structure of the Transition States and Intermediates Formed in the Water-Exchange of Metal Hexaaqua Ions of the First Transition Series. *J. Am. Chem. Soc.* **1996**, *118*, 6760–6766.
- (73) Brandt, S.; Sittel, F.; Ernst, M.; Stock, G. Machine Learning of Biomolecular Reaction Coordinates. *J. Phys. Chem. Lett.* **2018**, *9*, 2144–2150.
- (74) Wehmeyer, C.; Noé, F. Time-lagged autoencoders: Deep learning of slow collective variables for molecular kinetics. *J. Chem. Phys.* **2018**, *148*, 241703–10.
- (75) Berezhkovskii, A.; Szabo, A. One-dimensional reaction coordinates for diffusive activated rate processes in many dimensions. *J. Chem. Phys.* **2005**, *122*, 014503.